COMPUTER METHODS IN MATERIALS SCIENCE

2026, vol. 26, no. 1, 5–22
https://doi.org/10.7494/cmms.2026.1.1023

A Digital Twin for temperature prediction in the laser hardening process of NC10 steel

Piotr Lacki*, Anna Derlatka, Michał Lacki, Kuba Lachs

Czestochowa University of Technology, J.H. Dabrowskiego 69, 42-201 Czestochowa, Poland.

Abstract

In this study, Artificial Neural Networks (ANN) were created to develop a Digital Twin (DT) for temperature prediction in the laser hardening process of NC10 steel. The ANN were trained to predict temperature on the top layer during the laser hardening process of NC10 steel samples with different thicknesses and with various laser power and laser scanning speeds. The prediction developed during the project work was based on a parametric numerical model of the laser hardening process for a sample of NC 10 steel, using the Finite Element Method (FEM) within the ADINA software. Numerical simulations enabled a detailed analysis of the temperature produced on the surface of each sample, as well as a visualization of the structural changes made to the sample according to the laser hardening process. It is crucial to create data that reflects reality as closely as possible to assess the best setting for each process. A well created DT allows to make automatically important changes along laser hardening process. To obtain a set of the most efficient parameters for the desired result, Genetic Algorithms (GA) were integrated with the developed ANN. As a result, the authors developed an effective and efficient tool to predict the temperature produced along the laser hardening process.

Keywords: Digital Twin (DT), Artificial Neural Networks (ANN), Finite Element Method (FEM), laser hardening

1. Introduction

The concept of the Digital Twin (DT) was introduced over a decade ago (Negri et al., 2017). The terms Digital Twin refers to a virtual replica of physical objects, processes, or systems, continuously updated with real-world data (Sharma et al., 2022). This makes monitoring environments and devices easier, and enables simulations in virtual reality. Benefits include saving time and money, detecting production anomalies, and improving decision-making for future products and features. There are many definitions of a Digital Twin found in the literature, mainly because it is used in a wide range of areas. Despite this variety, most definitions share a common understanding that a Digital Twin consists of three key elements: the physical product, the virtual product, and the data that connects them. A Digital Twin is a great solution for analysing and optimising nonlinear dependencies.

Digital Twins can be represented in various forms, including theoretical models, numerical simulations, and artificial neural networks. Digital Twin has become a technology that is finding increased applications in different welding as well as additive manufacturing processes (Mu et al., 2023; 2025). In the study (Hegedűs-Kuti et al., 2025) data collected by the acquisition system during the welding process were combined with point cloud features obtained through structured light scanning

* Corresponding author
Authors' e-mails: piotr.lacki@pcz.pl, anna.derlatka@pcz.pl, michal.lacki3210@gmail.com, kublac24@gmail.com
ORCID ID's: 0000-0002-0787-8890 (P. Lacki), 0000-0002-6509-2706 (A. Derlatka), 0009-0007-7829-8192 (M. Lacki), 0009-0003-3567-6211 (K. Lachs)
Received: 30.05.2025, accepted: 15.09.2025, published: 2.01.2026

technology, along with seam width measurements derived from image recognition algorithms. This integration enabled an expanded approach to seam detection.

The authors of the paper (Lv et al., 2025) proposed a finite element model of resistance spot welding (RSW) to generate reliable synthetic data for a learning algorithm. This model effectively created a Digital Twin of the multi-physics phenomena, accurately simulating nugget growth, surface indentation, dynamic resistance, electrode force, and displacement signals.

On the other hand, the paper (Nayak et al., in press) introduces a hybrid Digital Twin model that integrates sensor data with physics-based simulations to replicate manufacturing scenarios. The model's effectiveness was demonstrated in the friction stir welding (FSW) manufacturing process.

Numerical simulations are widely used as representations of Digital Twins in various industries. Simulation modelling involves using a digital prototype to predict a physical system's real-world performance. Authors of the paper (Chen et al., 2021) proposed a method for creating a Digital Twin for friction stir welding using a sensor-based numerical simulation. They introduced an iterative cyber-physical fusion algorithm to calculate the in-process 3D temperature field by integrating measured temperature data with a 'moving heat source' analysis.

Laser hardening, which is increasingly used in industry, is performed to achieve a hard and wear-resistant surface layer. This technology is suitable for all materials that can undergo flame and induction hardening. Today, laser hardening is fully automated and allows the treatment of components with nearly any level of geometric complexity (Pakieła et al., 2020; Pawłowicz, 2014). Its application enables the processing of parts that, due to their design or function, could not be hardened using other methods. In the laser hardening process, only about 20% of the heat is introduced into the material compared to induction hardening. This significantly reduces the need for subsequent mechanical processing. Additionally, laser hardening allows for a relatively short operation time. During the process, the surface layer of the workpiece is heated to the austenitizing temperature, just below the material's melting point. Approximately 40% of the laser's emitted power is absorbed; however, in practice, the absorption rate depends on specific process conditions and the material's properties. To ensure effective laser hardening, tests are to select optimal laser parameters and to properly prepare the surface (Łach, 2024; Schüßler et al., 2023).

Currently, the engineering focuses on developing methods for simulations and optimization of different processes. For years, the finite element method (Derlatka & Lacki, 2024) and the method of fundamental solutions (Szczucka-Lasota et al., 2025) have been well-known. Methods of analysis of variance (ANOVA) (Lesyk et al., 2019), artificial neural networks (ANNs) (Lacki et al., 2024), genetic algorithms (GA) and statistically equivalent representative volume elements (SERVE) for microstructural characterisation (Rauch et al., 2020) are becoming more and more popular. Laser hardening modelling techniques encompass various approaches to predict and optimise process outcomes. These techniques are generally categorized into analytical methods, empirical models (Lesyk et al., 2023), FEM models (Schüßler et al., 2023), and data-driven models (Baronti et al., 2022), each providing specific insights and benefits (Łach, 2024).

This study presents DT for temperature prediction during the laser hardening process of NC10 steel. This steel is a traditional tool material commonly used for manufacturing tools designed for cold plastic forming. It is characterized by a high carbon and chromium content, as well as a significant amount of retained austenite after quenching from high temperatures (Berkowski & Borowski, 2007). A parametric numerical model based on the Finite Element Method (FEM) was developed to simulate the laser hardening process. This numerical model was then used to generate results for various process parameters. These data sets were subsequently applied to train an Artificial Neural Network (ANN).

2. Parametric FEM model

To analyse temperature variations in the material during the laser hardening process, a parametric FEM model was developed. Creating a parametric numerical model for the laser hardening process required incorporating key components to accurately reflect the physical phenomena occurring during material treatment. A laser beam modelling (using a Gaussian heat source), laser power, beam scanning speed, spot shape, and exposure time were considered in this study. The interactions with the external environment were also accounted by the model. The following properties: thermal conductivity $\lambda = 24.2$ W/m·K (at 700°C), specific heat capacity $c = 460$ J/kg·K, and the laser absorption coefficient on the sample surface were included in the thermal model for NC10 steel. The variable geometry of the sample was also incorporated in the model. Three-dimensional solid finite elements (3D Solid) were used, with the mesh element size not exceeding 1.6 mm. An example of the temperature distribution along with the sample dimensions was shown in Fig. 1.

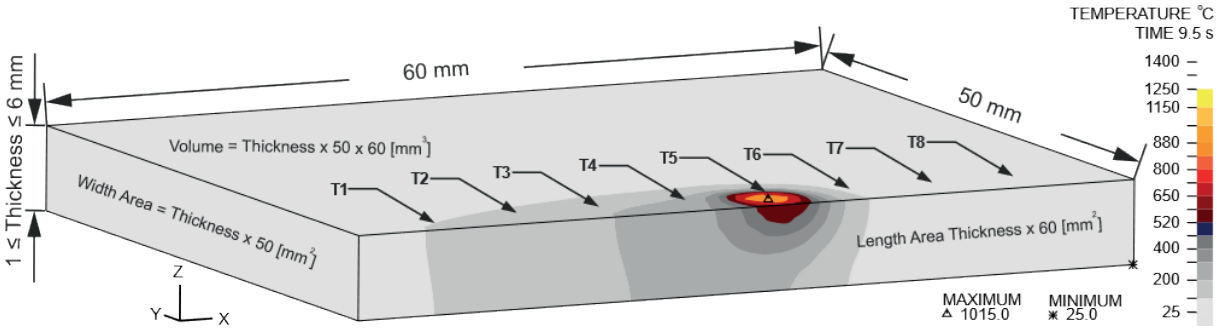

Fig. 1. The example of the temperature distribution on the surface of the analysed sample [°C]

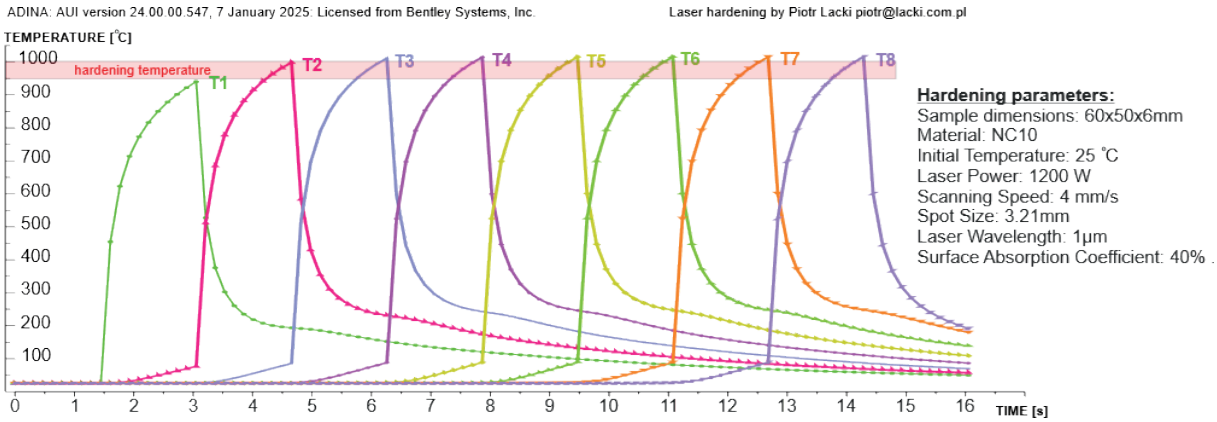

Fig. 2. The temperature variation [°C] over time [s] for the points T1–T8

The selection of parameters in the laser hardening process primarily depended on the type of material being treated, the thickness of the components, the performance requirements of the hardened element, and the type of laser used (Mahrle & Beyer, 2019; Mandolfino et al., 2020; Metzner et al., 2020). Precise control of all process parameters was crucial for achieving optimal results. Modern control systems enabled dynamic adjustment of parameters in real-time, allowing more efficient and effective hardening. However, accurately predicting the hardening temperature was not always possible. This temperature depended on the amount of energy delivered, the thermal conductivity of the material, and the changing thermal conditions within the hardened component. For NC10 steel, it was essential to precisely reach the target temperature range of 960–1000°C. Fig. 2 presents temperature variation graphs over time for measurement points T1–T8 in the analysed case study. The analysis shows that the lowest temperature was recorded at the first point T1, with a value of T1 = 940°C. At each subsequent point, the peak temperature slightly increased. The highest temperature was recorded at the final point (T8), reaching T8 = 1015°C.

In the hardening process, the cooling rate also plays a crucial role. Cooling typically occurs through natural heat dissipation into the surrounding cooler material (air cooling) (Czupryński et al., 2022). In the analysed case, the cooling rate did not fall below v_c = 700°C/s. Due to the rapid cooling, the material's structure did not revert to its original state, resulting in the formation of a very hard martensitic structure.

The maximum (peak) temperature reached during laser hardening on the sample surface was predicted by the neural network. The example FEM simulation presented in Fig. 1 and 2 show that in the studied case, the lowest measured temperature was about 940°C, while the highest was 1015°C at the last measurement point T8. The target range was assumed to be 960–1000°C (austenitic transformation temperature).

3. ANN architecture

The selection of the optimal neural network architecture depends on many factors, such as the type of problem, data availability, computational requirements, and the need for model generalization. Key aspects of this selection include data analysis, selection of layers and neurons, appropriate regularization techniques, and optimization strategy. There is no single universal

architecture. The selection requires experimentation, analysis of results, and application of appropriate parameter tuning, regularization, and optimization techniques. The strategies for determining the optimal ANN architecture adopted in this work are presented below.

3.1. Data preparation

The data presented herein were derived from a parametric finite element model and were selected to comprehensively capture the analysed range of the phenomenon under investigation while retaining practical usability. The total number of data points was directly influenced by the number of input parameters within the model. Specifically, a thickness variable parameter yielded 101 data points, the thickness and laser power parameters produced 143 data points, and the thickness, laser power and scanning speed parameters resulted in 572 records. The largest dataset, the training set, contains the highest number of records, which is critical for effective neural network training, as it is from this set that the inter-neuronal connection weights are learned. The validation set, with fewer records, was employed to monitor and stop the training process once signs of overfitting, a common occurrence when the training dataset is inadequate relative to the network's complexity.

The data selection methodology involved identifying records that define lower and upper bounds in each dimension to encompass all possible extremes, ensuring that the intervals between successive records were uniform. For dimensions such as sample thickness and laser power, each extreme was then adjusted inward by half the inter-record distance towards the median of the data spectrum. An analogous grouping strategy was applied to the laser scanning speed. This approach resulted in the generation of a secondary dataset from which the most representative records were ultimately chosen to form the validation and test sets. Fig. 3 presents the structure and proportions of the data sets used in the analysis. The proportions of these sets were determined based on the number of input neurons: for four inputs (Fig. 3a) the training set comprised 50% (50 records), the validation set 40% (40 records), and the test set 10% (11 records); for five inputs (Fig. 3b) the training set constituted 50% (71 records), the validation set 29% (42 records), and the test set 21% (30 records); and for six inputs (Fig. 3c), the training set included 50% (284 records), the validation set 29% (168 records), and the test set 21% (120 records).

Effective feature scaling is essential to accelerate convergence, increase numerical stability, and ensure reliable training of even the most extensive deep neural networks. In the analysed dataset, preserving the relative proportions of each feature while preventing extreme values from distorting the overall range was most important. Outliers can disproportionately stretch the input distribution, leading to vanishing or exploding gradients and unpredictable learning dynamics. To address this, the work adopts min–max scaling normalization, which linearly rescales all features to a fixed interval: [0, 1], thereby preserving the original relationships between observations, mitigating the impact of extreme values, and promoting smoother, more consistent optimization.

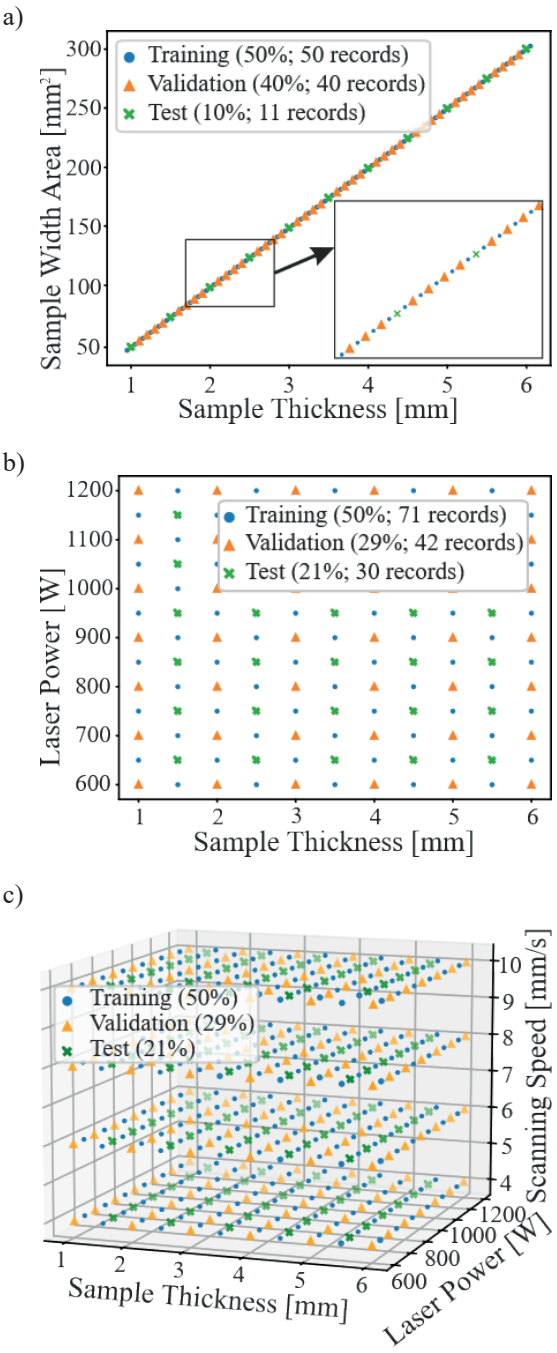

Fig. 3. Structure and proportions of the data sets used in the analysis: a) 4 input neurons; b) 5 input neurons; c) 6 input neurons

3.2. ANN model design

Choosing the right network architecture and topology is crucial to achieving the full potential of the ANN model. This selection is based on several considerations, primarily the nature of the input data, the complexity of the underlying problem, and the available computational resources. Fig. 4 shows sample configurations of ANN architectures used in the work: a) ID 1: 4-8-1, b) ID 5: 5-16-1, c) ID 9: 6-16-8-1.

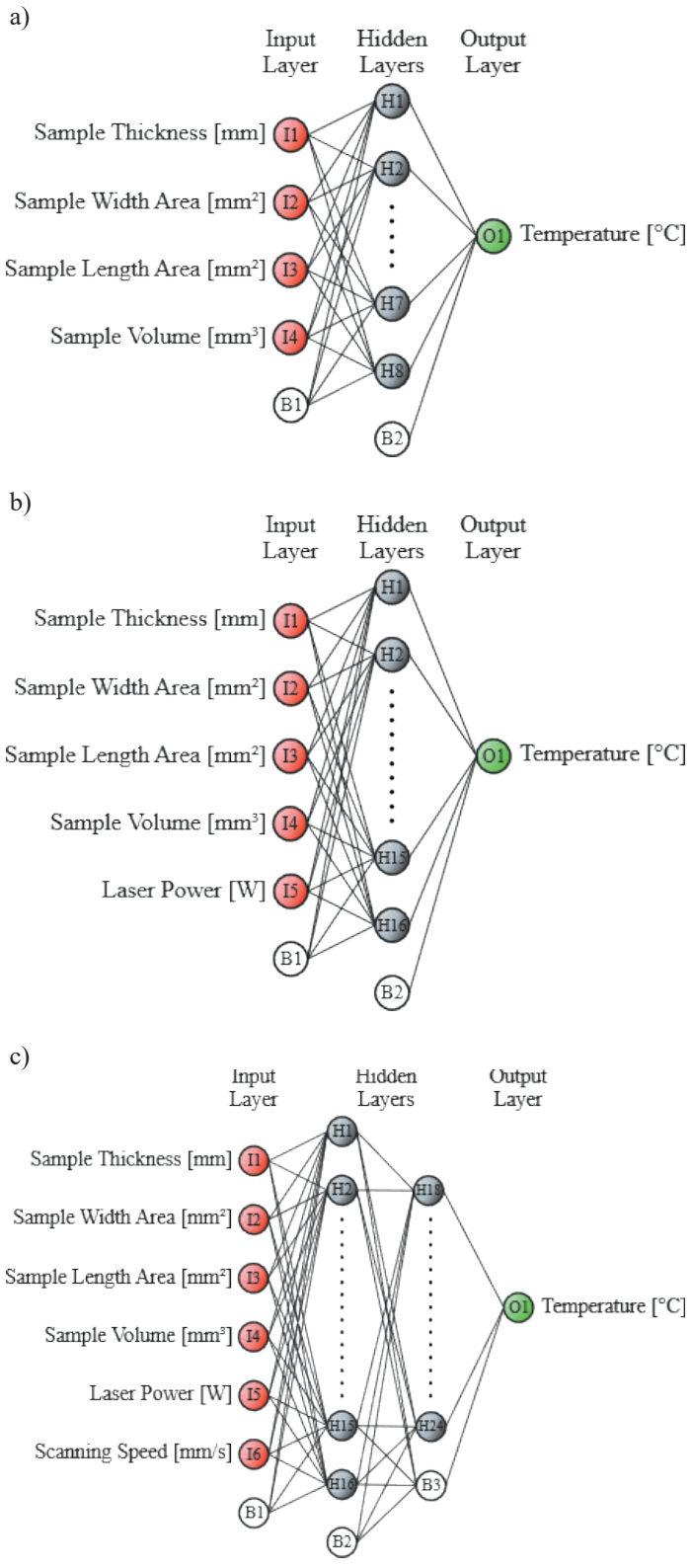

Fig. 4. Example ANN topologies used in the work: a) ID 1: 4-8-1, b) ID 5: 5-16-1, c) ID 9: 6-16-8-1

In the work, the task was a regression problem operating on structured numerical input data, which clearly indicated a Multilayer Perceptron (MLP) as the best solution. The input and output configuration comprised four input neurons and one output neuron. Next, three hidden-layer topologies were evaluated: the first employed a single hidden layer of eight neurons to distribute each input feature's importance across twice as many processing units; the second maintained a single hidden layer but expanded it to sixteen neurons, four times the size of the input layer, to achieve finer granularity in feature weighting; and the third introduced two hidden layers, the first with sixteen neurons to extract and allocate input feature importance and the second with eight neurons to generalize and refine those representations.

To assess sensitivity to dataset size, the effect of increasing the number of input examples on each topology's performance was investigated, yielding nine candidate architectures whose general specifications and post-training metrics were presented in Tab. 1. The loss function measured the error between predictions and actual values; for the regression case, the Mean Squared Error (MSE) was used. To evaluate the prediction results, the R squared (R^2) indicator was used as a quantitative indicator. All models were configured with a linear activation function in the input layer, a hyperbolic tangent activation function in the hidden layers, and a logistic (sigmoid) activation function in the output layer. Training was performed using backpropagation with a constant learning rate of $\alpha = 0.001$ and a batch size of one.

Table 1. General ANN specifications and metrics after network training

Architecture ID	Inputs	Topology	Number of epochs	Training time [s]	Training MSE	Validation MSE	Test MSE	R^2
1	4	4-8-1	484	69.93	0.025	0.022	0.039	0.9465
2	4	4-16-1	199	113.10	0.020	0.018	0.034	0.9554
3	4	4-16-8-1	1000	194.58	0.018	0.021	0.013	0.9853
4	5	5-8-1	998	135.40	0.028	0.046	0.035	0.9014
5	5	5-16-1	991	220.23	0.032	0.042	0.029	0.9298
6	5	5-16-8-1	999	375.37	0.028	0.033	0.025	0.9516
7	6	6-8-1	994	2052.52	0.038	0.048	0.028	0.8820
8	6	6-16-1	1000	3463.64	0.026	0.031	0.021	0.9371
9	6	6-16-8-1	1000	5567.17	0.022	0.028	0.017	0.9432

3.3. Training the model

In a regression-oriented deep network, a batch of input feature vectors X was first linearly transformed at each layer, then passed through nonlinear activations tanh, apart from the final layer in which the activation function was a logistic function. All operations are vectorized across the batch for efficiency. Once Y was produced, the mean squared error was computed to quantify prediction error, and the resulting scalar loss was used to drive subsequent backpropagation. During backpropagation, the network computes the gradient of the loss based on MSE with respect to each weight by applying the chain rule through all layers. Finally, the Stochastic Gradient Descent (SGD) algorithm updated each weight, taking into account the learning rate η. This vectorized process repeated each batch to gradually minimize the regression loss. To prevent overfitting, a simple but highly effective early stopping regularization was used. It monitors the performance of the validation set and stops training when convergence starts to deteriorate. No other regularization techniques, such as dropout or L1/L2 Regularization were used. Random initialization was used to set the initial weight values of neural networks to ensure efficient learning and stable gradients. The random values from a uniform distribution in the interval [0, 1] were assigned to the initial weight values.

3.4. Model validation and hyperparameter tuning

The model was validated using early stopping. For this purpose, a validation set was first reserved, which the network never sees when updating the weights. After each training epoch, the validation loss (MSE) was calculated and compared to the best obtained value. If the loss did not improve for a fixed number of consecutive 10 epochs, training was stopped to prevent overfitting. Then, the weights of the model with the lowest validation loss were restored. By preventing further updates

that would only reduce training loss at the expense of validation accuracy, early stopping curbs overfitting and often yields a model that generalizes better to unseen data. Fig. 5a shows the Mean Squared Error (MSE) for the training set (blue), validation set (orange), and test set (green) as a function of training epoch. The plot refers to the ID 1: 4-8-1 neural network architecture. All three curves first decline sharply and then slowly converge to a low plateau. The vertical red line marks the epoch (around 500) at which training was stopped (via early stopping), showing that at this point the model error on the training, validation, and test data has essentially plateaued, and further training did not yield any real improvement. Similar relationships for the learning curves could be observed in Fig. 5b and c for the ID 5: 5-16-1, and ID 9: 6-16-8-1 network architectures, respectively. Convergent validation and test curves (parallel decline and plateau at similar levels) confirmed that validation was a good approximation of performance on unseen data.

The random search used in this work started by defining a uniform sampling distribution for each hyperparameter. Instead of evaluating each point on a fixed grid, the random search simply draws a value for each hyperparameter from its corresponding distribution. After each 10 models, which were trained and evaluated, the sample with the best validation performance was selected for final testing or deployment. Because the random search allocated more trials to parameters that actually affect performance (rather than wasting effort on less sensitive ones), it often found a near-optimal configuration with fewer experiments than the full grid search. The basic ANN hyperparameters used in this work are presented in Tab. 2.

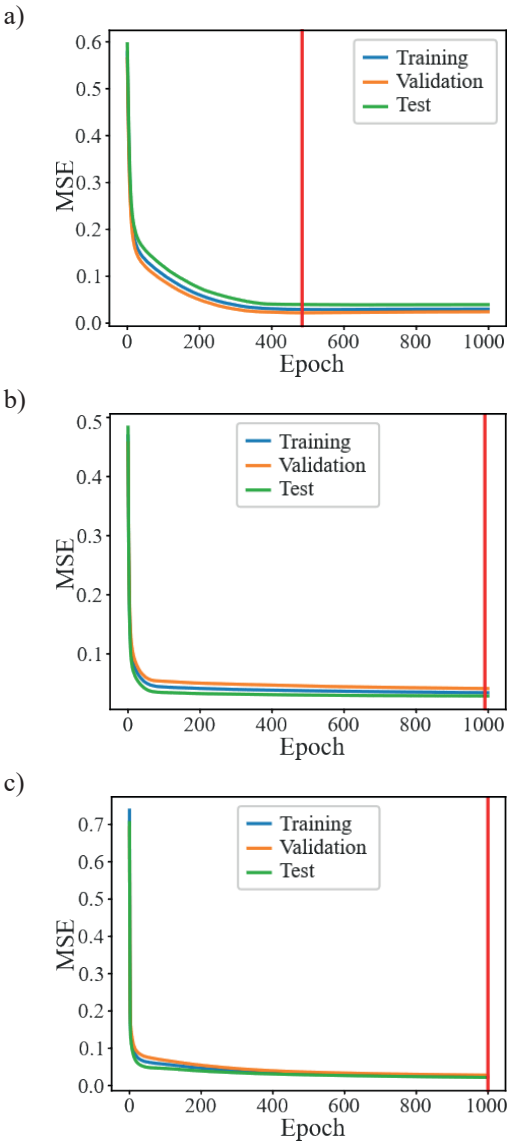

Fig. 5. Learning curves MSE vs. epoch plots for ANN models: a) ID 1: 4-8-1; b) ID 5: 5-16-1; c) ID 9: 6-16-8-1

Table 2. Basic hyperparameters of the ANN used in the work

Hyperparameter	Value	Concise description
Hyperparameter fine-tuned technique	random search	Randomly testing different hyperparameter values
Learning rate (α)	0.001	Controls the step size during optimization. A higher value speeds up learning but may cause instability, while a lower value ensures stability but slows training
Batch size	1	The number of training examples used in one forward and backward pass. A larger batch improves stability but requires more memory.
Epochs	max. 1000	The number of times the entire dataset is passed through the network during training. More epochs can improve accuracy but may lead to overfitting
Weight initialization	random initialization	Assigned small random values from a uniform distribution in the interval [0, 1]
Activation function	input: linear hidden: tanh output: logistic	Defines how neurons transform input signals

Table 2 cont.

Hyperparameter	Value	Concise description
Regularization	early stopping	Prevents overfitting by not training for too long
Optimizer	SGD	Stochastic Gradient Descent (SGD), algorithm that updates weights based on gradients
Number of hidden layers	1–2	Determines the depth of the network, affecting its ability to learn complex patterns
Number of neurons per layer	input: 4-6 hidden: 8-16 output: 1	Defines the capacity of each layer to extract features from input data
Loss function	MSE	Measures the error between predictions and actual values

3.5. Model testing

To ensure that the model generalizes well and is not only suitable for validation, the model metrics were compared in the validation and test sets. Fig. 6a shows the absolute error AE, which is the difference between the data generated from FEM and fed into the ANN input and the data obtained after training the ANN on the sample thickness as a function of temperature for the example architecture ID 1 with the 4-8-1 topology. To evaluate the accuracy of the ANN, the discrepancy field was used. In Fig. 6b, the discrepancy field is shown between the blue line representing the FEM input value and the orange line representing the prediction data for the example architecture ID 1 with the 4-8-1 topology.

Decisions regarding changes to the architecture were based on the validation results, avoiding looking at the test metrics until the final evaluation. If the validation error decreased after reaching a training plateau, another hidden layer was added to increase the model capacity, allowing the network to learn more complex features. When the model was underfitted and the validation error was high and not reduced, the number of neurons in the hidden layers increased. When the model was overfitted, the training error was low, but the validation error was high, the number of neurons was reduced.

The scatter of points around the red line in Fig. 7 indicates prediction errors. Systematic deviations from the red line indicate decreasing prediction range. If the points form curves or shapes other than a straight line, the model may have trouble capturing relationships or may not be well-fitted to the data. The scatter plot complements numerical metrics, showing the distribution of errors that numbers alone (e.g. MSE, R^2) do not reveal. In addition, it helps detect outliers, single points far from the line suggesting outliers or cases that are difficult to predict.

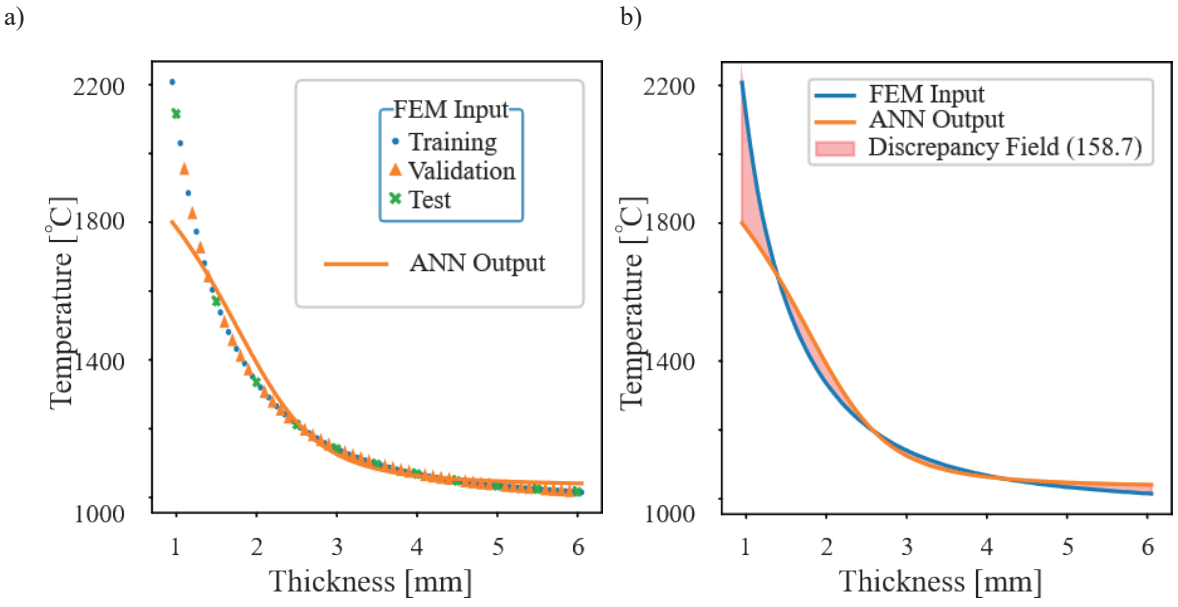

Fig. 6. Graph of temperature change vs. sample thickness: a) absolute error; b) discrepancy field

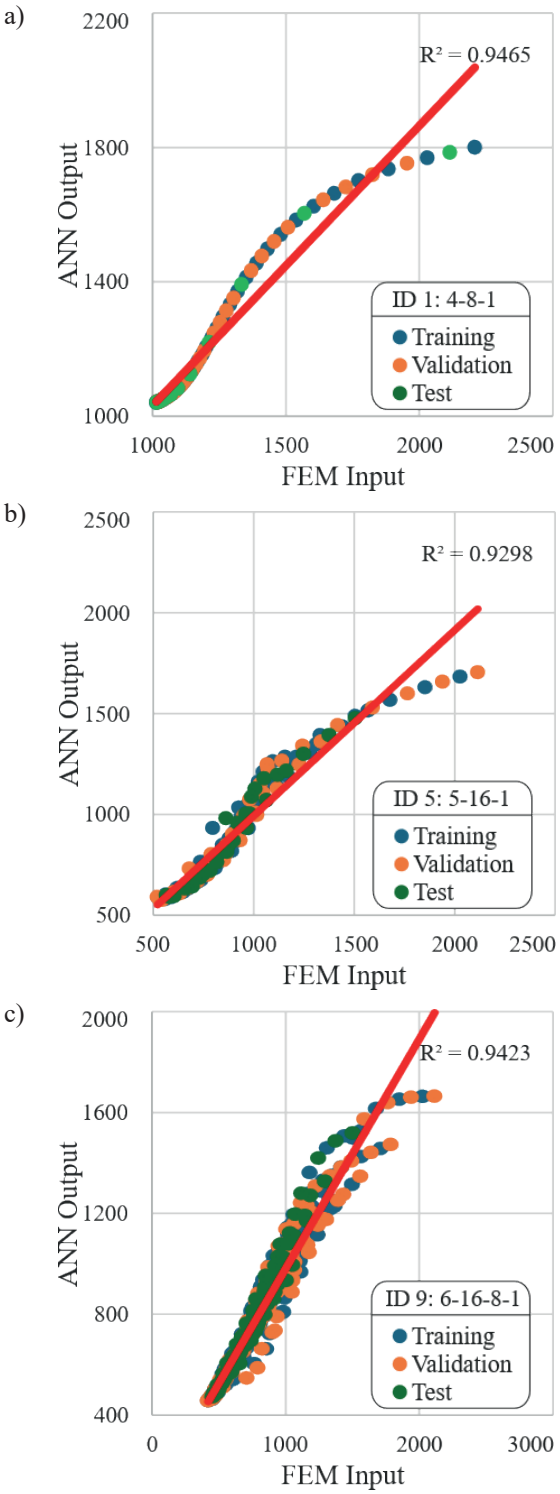

Fig. 7. Scatter plots of FEM input vs. ANN output: a) ID 1: 4-8-1; b) ID 5: 5-16-1; c) ID 9: 6-16-8-1

3.6. ANN results

Fig. 8 shows the results from the training analysis of a 5-16-1 topology neural network. Fig. 8a is a map of the network training values, generated from the FEM model. Fig. 8b is a map of the neural network predictions, where the values come from ANN calculations, Fig. 8c is a map of the difference between the values calculated from the FEM parametric model and the neural network. The maps presented in Fig. 8a and b show a good fit of the temperature distribution shape. In both the low temperature regions (top left) and the high temperature regions (bottom right), the isotherms are visually similar. This indicates that the ANN network has successfully learned to predict the relationship between the input parameters (laser power, thickness) and the final temperature obtained from the FEM simulation. The absolute error (Fig. 8c) is dominated by dark (low) shades in most of the AE region <60°C, which in the temperature range from 400°C to 2200°C is a relative error of the order of several percent. The average error is within acceptable limits for engineering applications. Local foci of higher deviations appear in narrow parameter bands (e.g. thickness ≈3 mm and power ≈800 W or thickness ≈5–6 mm at power 1000–1200 W). These may be areas where the FEM model exhibits non-stationary or strongly nonlinear transitions, which are more difficult to accurately capture by a single-layer network. However, the maximum deviation (~400°C) occurs only in small, marginal regions of the parameter space (very small thickness ≈1 mm at 1000–1200 W).

The 5-16-1 topology proved to be sufficient to obtain a high level of compatibility with the FEM model at a low computational cost. In summary, the 5-16-1 network emulates the temperature distribution from the FEM model very well (average error of a few percent), and the observed local deviations indicate areas where the model capacity can be increased. In order to reduce absolute errors in critical regions, adding more hidden layers and increasing the number of neurons to better capture local, nonlinear phenomena was tested.

The network prediction map shown in Fig. 9b correctly reproduces the gradients and isotherms visible in the FEM simulations Fig. 9a. Both at low laser powers and low scanning speeds and at high ones, the relative structure of the horizontal temperature transitions is preserved. This indicates a good fit of the overall shape of the temperature distribution. The error scale in Fig. 9c map shows that in the majority of the AE parameter space, it oscillates below 20°C, which in the temperature range of 400–1200°C is <2% of the relative error. The maximum deviations (of the order of 60–70°C) appear only in narrow areas of the extreme combinations (the highest powers at high scanning speeds). In general, it can be stated that low absolute errors are observed in most areas. Compared to the simpler 5-16-1 topology (Fig. 8), the 6-16-8-1 network shows significantly lower maximum errors (70°C vs. ~400°C). This means that

adding the layer and neurons significantly improved the model's ability to capture strong nonlinearities in the extreme parameter regions, which translated into a reduction of local peaks in absolute error.

The second hidden layer (8 neurons) allowed the better modelling of the complex dependencies between the six inputs and the output temperature. The greater depth (2 layers of 6-16-8-1 instead of 5-16-1) significantly reduced both the mean and maximum error – indicating a better capacity of the network to approximate FEM functions with a small increase in computational cost. Maintaining a moderate layer width (16 neurons in the first layer) provided a good balance between the model's ability and the risk of overfitting.

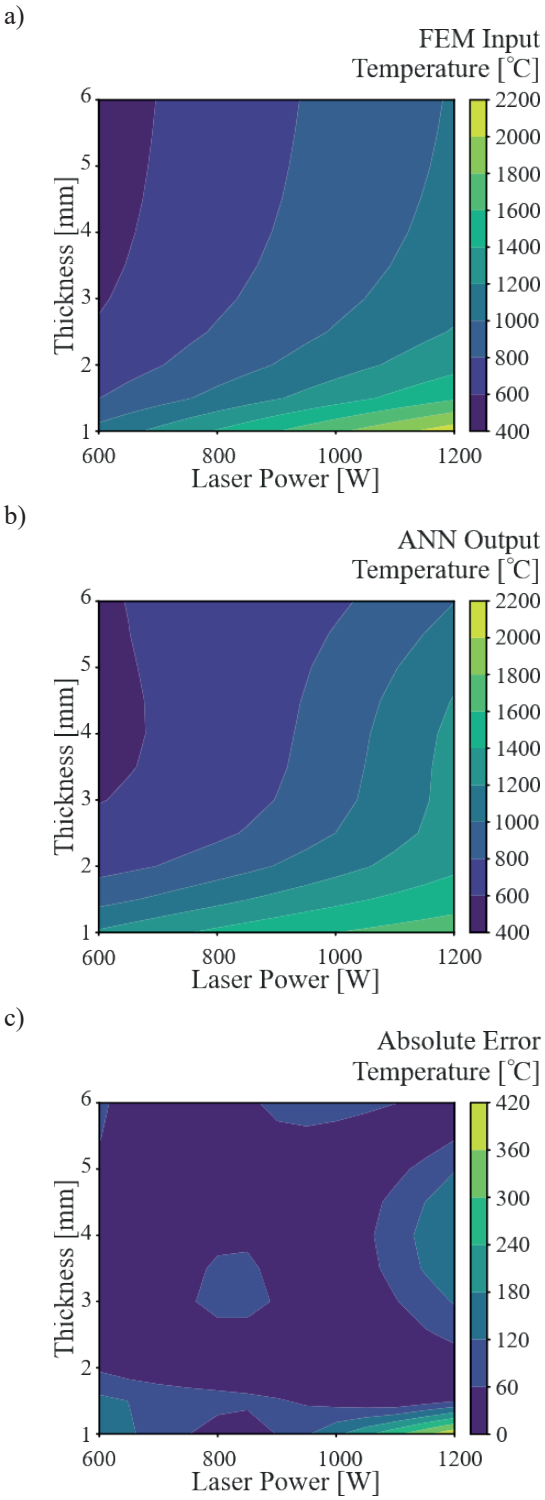

Fig. 8. Results for an ANN ID 5 with the topology 5-16-1: a) FEM input data; b) ANN output data; c) absolute error

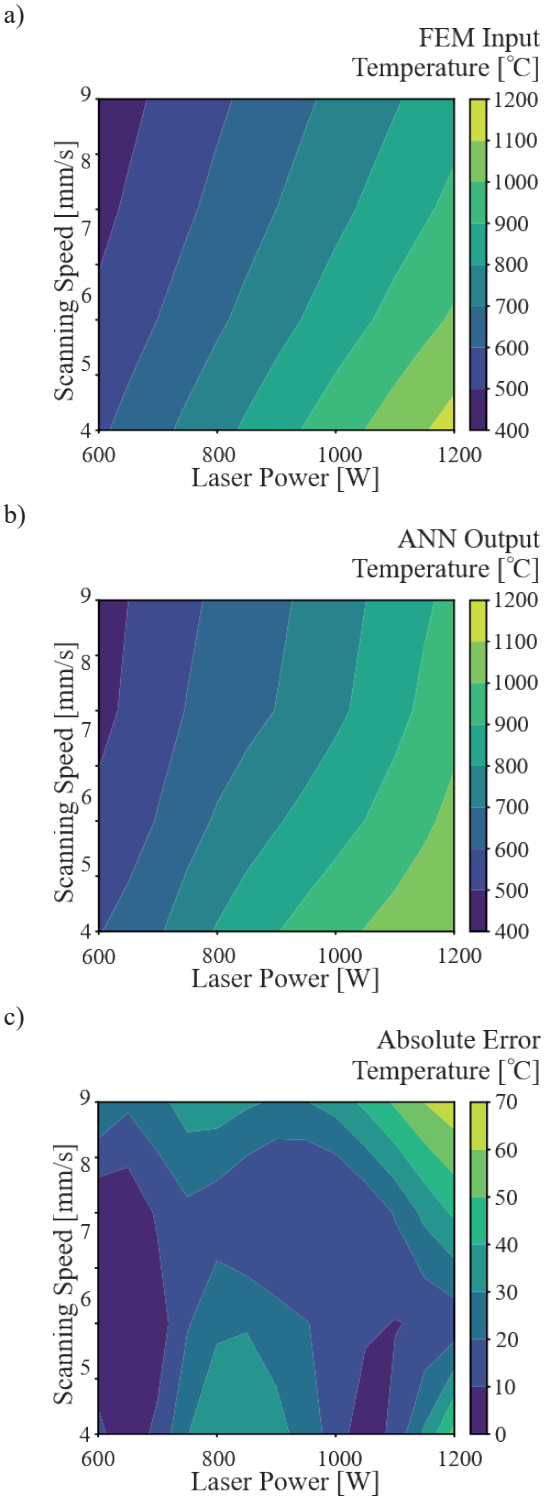

Fig. 9. Results for an ANN ID 9 with the topology 6-16-8-1: a) FEM input data; b) ANN output data; c) absolute error

3.7. Recommendations for further development of the ANN architecture

Adding more neurons in the second layer from 8 to 16 neurons could even better capture local transitions in areas where the error reaches ~60°C. Adding another hidden layer e.g. 6-16-8-4-1 (or 6-32-16-8-1) topology would give the model greater depth and capacity to model highly nonlinear regions. Introducing residual connections (skip connections) will allow for easier training of deeper networks and stabilization of gradient flow, which is useful when adding layers.

Better tuning of optimization hyperparameters, in particular a lower learning rate + learning-rate decay, will help to more accurately match in areas of high nonlinearity. Batch normalization between layers will speed up convergence and may additionally reduce AE.

The use of local specialized models is also planned. If the edge regions (where the error is the largest) are crucial, you can train small networks specialized on these parts of the parameter space and mix their predictions with the main model.

Implementing the above changes should allow the further reduction of the absolute error, especially in the most demanding parameter regions.

4. Optimization with GA

Another important aspect of the research is the optimization of the hardening process using genetic algorithms (GA). The flowchart showing how the GA optimizer interacts with the ANN was presented in Fig. 10.

The first step involved using a neural network trained on historical FEM simulation data, whose task is to predict the maximum temperature in the hardening zone depending on input parameters – such as laser power, scanning speed, sample thickness, or type of cooling. Then, this fast prediction method becomes DT in the pool of individuals of the genetic algorithm, where each individual represents a specific combination of values of these parameters.

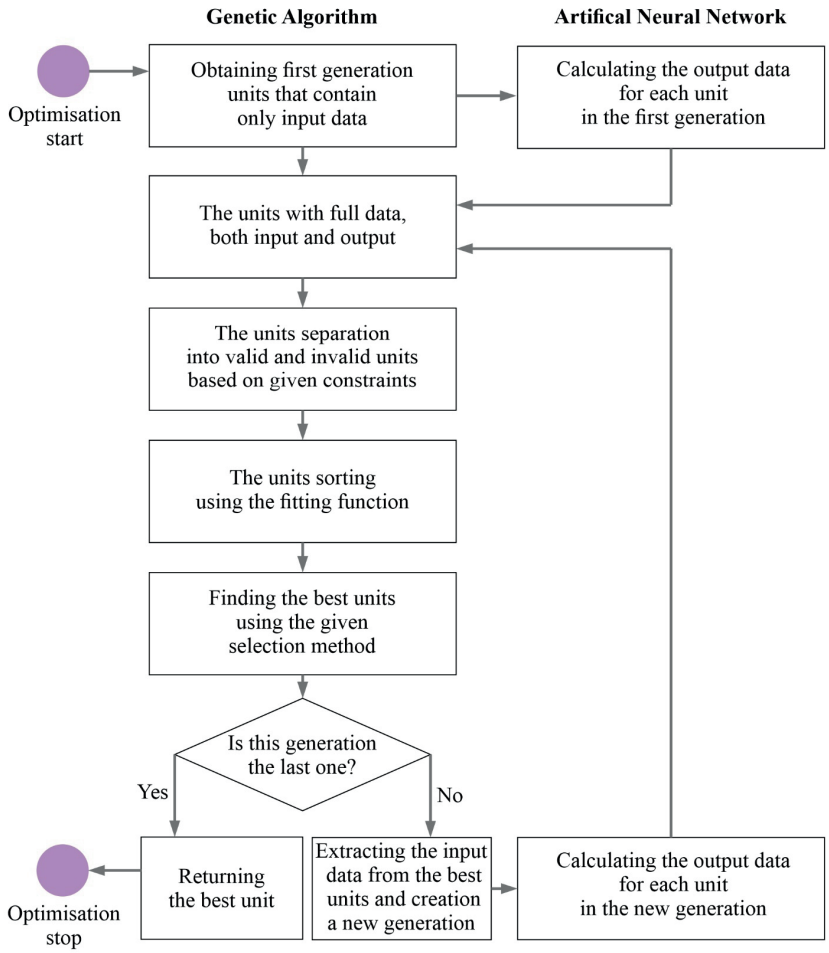

Fig. 10. Flowchart showing how the GA optimizer interacts with the ANN

The entire optimization process was carried out while taking into account physical and technological constraints: for example, laser power ranges (600−1200 W), permissible scanning speeds (4−9 mm/s) or the maximum sample thickness (1−6 mm) which can be subjected to hardening. In practice, these constraints were implemented as rejection conditions in the phase of generating new individuals. Ultimately, after conducting 1000 generations, the genetic algorithm returned the optimal or suboptimal set of input parameters. Such a result allowed not only for the significant acceleration of laboratory experiments, but also for an economically and technologically optimal design of the hardening process while maintaining all the necessary constraints.

The genetic algorithm began its evolution by generating a random population of the parameter set for the first generation. Depending on the ANN architecture used, the population size was 8, 16, or 32 individuals. For each set, the fitness function value is calculated, which were defined in order to, for example, minimize the maximum temperature (to reduce stress) or, on the contrary, maximize the temperature to quickly obtain the desired material structure. Thanks to the use of genetic operators, the selection of the best solutions, crossover, and mutation, subsequent generations adapted better and better to the optimization criterion. Tab. 3 shows the important GA hyperparameters used in the work.

Using crossover rate = 1 (100% probability of crossover) means that every pair of selected parents is crossed, without exception. Using such a value makes sense in the case of high pressure to explore the solution space, when it is necessary to quickly search for new combinations of features and increase the diversity of offspring and to maximize the potential of mixing genes in the population. Using such a value of the Crossover Rate requires a well-designed elitism mechanism. In this work, an elitism rate = 25% was used. If elitism is applied and the best individuals are copied without changes, aggressive crossbreeding of the remaining population can be allowed. Crossover rate = 1 makes sense and is effective, because care was taken to preserve the best individuals for the next population. If selection pressure is too strong, meaning that only the very best individuals are consistently chosen for reproduction, diversity in the population can rapidly decrease. In such cases, a higher mutation rate can introduce new genetic material, preventing stagnation in local optima. In problems where the population size is very small, genetic diversity is naturally low. A higher mutation rate ensures that the algorithm introduces more variety to compensate for the lack of genetic diversity from crossover alone. In this work, a mutation rate = 50% was used, which is extremely high for most genetic algorithms and is generally not recommended. However, whether it can be used depends on the type of problem and implementation. In the case of small populations, when genetic diversity is low, a high mutation rate can introduce more variability. In real-valued genetic algorithms, mutation often involves Gaussian perturbation instead of flipping bits. In some cases, a higher mutation probability can help escape local optima without completely destroying beneficial traits.

Table 3. Relevant hyperparameters of the GA used in the work

Hyperparameter	Value/range/options	Description/ comments
Population size	8-16-32	number of individuals in each generation
Genome size	3	number of genes in an individual's genome
Encoding scheme	real-valued	representation of the decision variables
Number of generations	1000	total iterations the GA will run through to evolve solutions; total number of generations before stopping
Selection method	tournament	How individuals are chosen for reproduction
Tournament size	4	number of individuals randomly chosen to compete for selection
Crossover type	one-point	type of crossover used (e.g., one-point, two-point, uniform)
Crossover rate	1.0	probability of crossover occurring between parents
Mutation type	swap	type of mutation applied (e.g., bit flip, swap, Gaussian noise)
Mutation rate	0.5	probability of mutating a gene
Replacement strategies	elitism	The best individuals from the previous generation are preserved in the new population
Elitism rate	25%	The percentage of the best individuals in a population that are retained in the next generation without modification
Termination criteria	fixed generations	Conditions under which the GA stops running. Prevents unnecessary computation once an optimal solution is reached

4.1. First GA optimisation

The aim of the first GA optimization of the hardening process was to determine the thinnest sample t [mm] suitable for laser hardening at a laser power of P = 1200 [W] and scanning speed v = 4 [mm/s]. The optimization was performed with a temperature limit of T [°C] in the hardening range. The fitting function minimized the sample thickness t [mm]. With the following assumptions:

- constraints:
  - 960°C ≤ T ≤ 1060°C,
  - 1 mm ≤ t ≤ 6 mm,
  - P = 1200 W,
  - v = 4 mm/s;
- fitting function: $f(t) = 1/t$;
- GA results:
  - T = 1060°C,
  - t = 4.15 mm,
  - P = 1200 W,
  - v = 4 mm/s,
  - width area: 207.5 mm^2,
  - length area: 490 mm^2,
  - volume: 12,450 mm^3.

Fig. 11 shows the temperature in the hardening zone as a function of sample thickness t for the established process parameters (P = 1200 W, v = 4 mm/s). Each point corresponds to the ANN prediction. Red points ("above range") – thicknesses too small, leading to a temperature of >1060°C, blue points ("below range") – thicknesses too large, leading to a temperature of <960°C, green points ("in range") – thicknesses ensuring a temperature within the hardening range of 960–1060°C, yellow star ("optimum") – solution selected by GA to minimize the sample thickness, but at the same time meeting the restriction of 960°C ≤ T ≤ 1060°C.

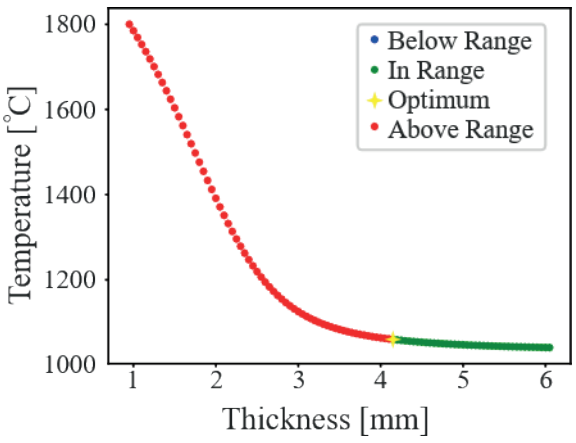

Fig. 11. Results of the first GA optimization of the hardening process

With decreasing sample thickness, the temperature increases rapidly (over 1800°C for t = 1 mm), and with increasing thickness, the temperature gradually approaches the minimum level of approx. 1000°C. The green points mean that at P = 1200 W and v = 4 mm/s the temperature is within the hardening zone for $t \gtrsim 4.0$ mm. Below this value, the temperature exceeds 1060°C; above – it drops below 960°C. The genetic algorithm, minimizing the fitness function $f(t) = 1/t$ with the imposed constraints, indicated the thinnest allowable sample as t = 4.15 mm. At this point, the temperature is T = 1060°C, exactly at the upper limit.

4.2. Second GA optimization

The aim of the second GA optimization of the hardening process was to find the thickest sample t [mm] using the lowest possible laser power P [W] and a constant scanning speed v = 4 mm/s at which laser hardening occurs on the sample surface. With the following assumptions:

- constraints:
  - 960°C ≤ T ≤ 1000°C,
  - 1 mm ≤ t ≤ 6 mm,
  - 600 W ≤ P ≤ 1200 W,
  - v = 4 mm/s;
- fitting function: $f(t) = t + 1/P$;
- GA results:
  - T = 969°C,
  - t = 6 mm,
  - P = 1180 W,
  - width area: 300 mm^2,
  - length area: 360 mm^2,
  - volume: 18,000 mm^3.

Fig. 12 shows the parameter space (P, t) divided into three areas. The red area ("above range") is the temperature range predicted by ANN where T > 1000°C and there is a risk of overheating. The blue area ("below range") is T < 960°C where there is insufficient heating for hardening. The green area ("in range") is 960°C ≤ T ≤ 1000°C, the allowable hardening range. The yellow asterisk indicates ("optimum") the result of GA minimizing the function $f(t, P) = t + 1/P$ (the function tends to the largest possible thickness and the lowest possible power). The green band on the graph is a narrow zone of allowable combinations (P, t) in which surface hardening occurs (960–1000°C). In order to obtain the largest possible sample thickness at the lowest possible power, the genetic algorithm aims at the extreme point of this band in the upper right corner – where t is maximum and P is minimum within the green area.

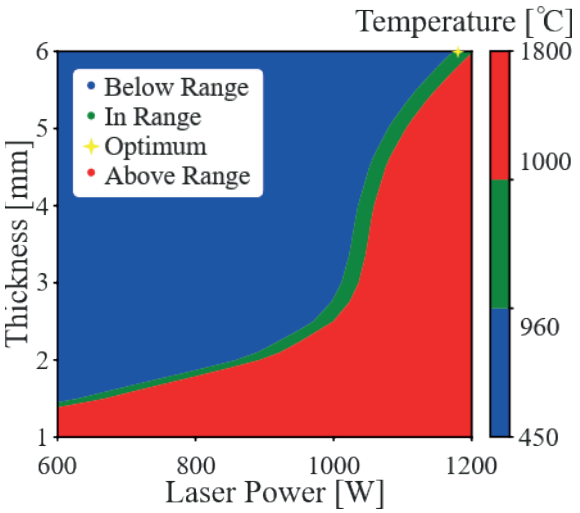

Fig. 12. Results of the second GA optimization of the hardening process

The optimal solution occurs at a thickness of $t = 6$ mm (maximum of the allowable range), and the laser power is the minimum value allowing hardening at this thickness, i.e. $P = 1180$ [W]. For these parameters, the ANN network gives a temperature of $T = 969$°C, just above the lower threshold, ensuring effective hardening without the risk of overheating. The GA chose $t = 6$ mm because each smaller layer would give a lower f, and a larger thickness (impossible) would exceed the physical limits. Although the goal was to use the lowest possible power, at $t = 6$ mm ANN models indicate that the temperature reaches the lower limit of 960°C only close to $P = 1180$ W. Lower powers would give the blue "below range" area. From the perspective of process safety, selecting a point just at the lower hardening limit (969°C) provides some margin, we do not risk overheating ($T > 1000$°C), and at the same time, we use a relatively large amount of material, which was a priority in this optimization. The second optimization successfully determined the thickest allowable sample at the lowest possible power, guaranteeing hardening with minimal risk of overheating.

4.3. Third GA optimization

The aim of the third GA optimization process is to determine the lowest scanning speed v [mm/s] and the weakest laser power P [W] suitable for laser hardening at a sample thickness $t = 3$ [mm]. With the following assumptions:

- constraints:
  - 960°C ≤ T ≤ 1000°C,
  - 4 mm/s ≤ v ≤ 9 mm/s,
  - 600 W ≤ P ≤ 1200 W,
  - $t = 3$ mm;
- fitting function: $f(t) = 1/P + 1/v$;
- GA results:
  - $T = 963$°C,
  - $t = 3$ mm,
  - $P = 990$ W,
  - $v = 4$ mm/s,
  - width area: 150 mm^2,
  - length area: 180 mm^2,
  - volume: 9000 mm^3.

The division of the two-parameter space (P, v) for a constant sample thickness $t = 3$ can be seen in Fig. 13. The red colour ("above range") indicates the temperature area where $T > 1000$°C (overheating). The blue colour ("below range") indicates the temperature area where $T < 960$°C (too low heating), the green area ("in range"): 960 ≤ T ≤ 1000°C is the allowable hardening zone. The yellow star ("optimum") indicates the result of the GA minimizing the function $f(P, v) = 1/P + 1/v$. The genetic algorithm indicated ($P = 990$ W, $v = 4$ mm/s) – i.e. the lowest power and the lowest speed, which led at $t = 3$ mm to a temperature of $T = 963$°C, just above the lower hardening limit. The graph shows that for lower powers or higher speeds (blue area) T drops below 960°C.

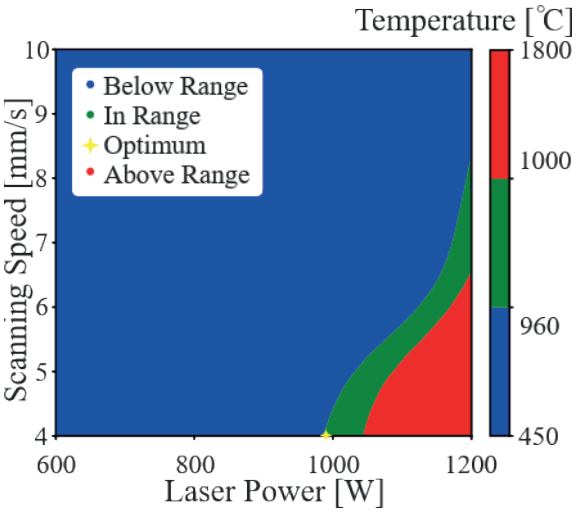

Fig. 13. Results of the third GA optimization of the hardening process

The narrow zone of permissible parameters means that the hardening parameters must be precise, because small deviations quickly take the process outside the hardening range. The optimum point lies just at the lower limit of 960°C, which minimizes energy consumption, but with process uncertainties it can risk underheating. The third optimization effectively indicated the absolute minimum of power and speed for $t = 3$ mm,

but in practice it is worth considering small corrections to avoid the risk of underheating in conditions of process variability.

5. Digital Twin

Digital Twin is a virtual replica of a physical process or system that reflects its real-time behaviour using measurement data and advanced simulation models. In this study, the development of the Digital Twin was achieved by combining precise Finite Element Method (FEM) simulations with a predictive model in the form of Artificial Neural Networks (ANN).

The ANN model acted as a fast equivalent to expensive FEM calculations, allowing for near-instantaneous prediction of the temperature distribution in the laser hardening process. Error analysis indicated that the largest deviations occurred at the extremes of the parameter space, suggesting that further refinement of the training set or expansion of the network architecture could further improve the accuracy. Fig. 14 shows the use of DT to determine the hardening volume zone in NC10 steel.

An integral part of this framework was an optimization layer based on Genetic Algorithms, which cooperates with both the Digital Twin and the neural network to systematically explore the multidimensional hardening parameter space. This allowed the simultaneous implementation of multi-criteria goals – maintaining the desired material microstructure, minimizing surface defects, and optimizing energy consumption.

Such synergistic integration of DT, ANN, and GA enabled adaptive process control in real time: based on measurement signals, the Digital Twin updated its forecasts, ANN provided immediate results, and GA dynamically selected parameters to continuously improve processing efficiency and quality. This creates a closed cycle of autonomous improvement that significantly accelerates the implementation of new production technologies and ensures their flexibility in changing operating conditions.

6. Discussion

In the current Artificial Neural Network (ANN) model used to predict laser hardening parameters, only static input data were taken into account, such as thickness, width, length and volume of the sample, as well as laser power and scanning speed. The temperature variation over time, which is a significant factor influencing the quality of the hardening process, was not directly considered by the model. This is particularly important in the context of the movement of the heat source (laser beam) and the slow accumulation of thermal energy on the surface of the sample. Therefore, the thermal history of the material was not reflected by the ANN model, which can lead to inaccurate predictions in cases where the influence of previous laser passes was significant.

In the context of Digital Twin (DT) or Digital Shadow (DS) systems, taking into account the dynamics of temperature distribution over time could significantly increase the accuracy and usability of the model. The integration of genetic algorithms (GA) with information on the temperature course of the sample would create the possibility of dynamic adjustment of process parameters (e.g., laser power or scanning speed) in real-time. This would avoid undesirable phenomena such as material overheating, while optimizing energy efficiency and the final quality of heat treatment.

At the current stage of research, the temperature predicted by the ANN network referred to the peak value at a specific spatial and temporal point. In the case where the temperature was only an intermediate result calculated based on other parameters, extending the model with a sequential or recursive component (e.g. LSTM), which would allow for the inclusion of time dependencies, were considered.

Indeed, Fig. 8 reveals clear differences between the ANN results and the Finite Element Method (FEM) simulations, which are considered as the reference, indicating the limitations of the current version of the ANN model in terms of generalization and accuracy.

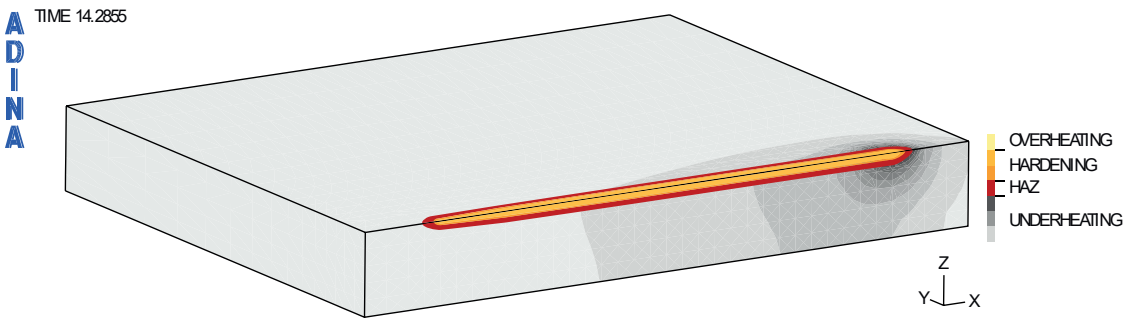

Fig. 14. DT prediction to determine the hardening volume zone in NC10 steel

However, it is worth noting that these discrepancies are due to several factors, such as:

- insufficient or unevenly distributed training data in the regions of extreme parameter values;
- too simple network architecture not adapted to the complexity of the process;
- inappropriate loss function or metrics during training;
- lack of validation data covering the entire range of physical parameters.

Discrepancies between the analysed FEM and ANN models can be treated as clues for further optimization, e.g. by expanding the training dataset, using deeper or hybrid networks, and techniques such as active learning. Ultimately, despite its current inaccuracies, the ANN model can still be a useful decision support tool, especially in combination with FEM simulations and genetic algorithm optimization. However, it is important that its limitations are explicitly identified and taken into account when interpreting the results.

The influence of temperature history on the quality of prediction will be analysed by the Authors in further studies combined with the experiment. It will be justified to clearly present the results of experimental studies as a validation of the model. The integration of the time component is indicated by the Authors as one of the priority directions for further research in the perspective of developing a Digital Twin of the laser hardening process.

In the next stages of development of the proposed system, an important research direction will be the full integration of the trained Artificial Neural Network (ANN) model and the Genetic Algorithm (GA) with the actual laser hardening system. The aim of these activities is to create a Digital Twin (DT) – an advanced digital environment that faithfully reproduces the physical process in real time, enabling both prediction of the system's behaviour and its optimization.

As part of this integration, it is planned to implement a feedback loop in which the temperature predictions generated by the ANN will be continuously compared with the actual data obtained from sensors (e.g. pyrometers, thermal imaging cameras). This architecture will allow for dynamic adjustment of process parameters – primarily laser power and scanning speed – in order to avoid material overheating and ensure conditions consistent with the requirements of the hardening process.

An important aspect of future work will also be the physical validation of the digital model. Experimental studies are planned with the participation of real material samples, in which the process features predicted by the model (e.g. temperature, depth of the hardened layer) will be compared with measurement results (e.g. microhardness, metallographic analysis, 3D measurements). This approach will enable further calibration of the model and increase its reliability and accuracy.

To sum up, the further development of the system should aim at a fully autonomous and intelligent laser hardening process control environment based on data, artificial intelligence and physical-digital integration. This approach is consistent with the concept of Industry 4.0 and can serve as the basis for a broader implementation of Digital Twins in material heat treatment technology.

7. Conclusions

The Digital Twin presented in this work for laser hardening was the methodology with immense potential, combining real-time modelling, simulation, autonomy, machine learning, prototyping, optimization, and big data. One of the key advantages of the Digital Twin is its speed of action, while a limitation lies in the generation and processing of large volumes of data. Based on the analyses conducted using DT, the following conclusions were drawn:

- The ANN models successfully capture the general temperature distribution, though minor inaccuracies appear at small thicknesses and high laser power.
- First optimization showed that thickness $t = 4.15$ mm is the thinnest sample thickness that provides hardening conditions on the surface, and occurs at laser power $P = 1200$ W and scanning speed $v = 4$ mm/s. Above this thickness, the temperature on the surface that goes beyond the hardening range was obtained, and below this thickness, the hardening temperature was within the range of hardening conditions.
- Second optimization showed that at the scanning speed of $v = 4$ mm/s, for the thickest sample plate $t = 6$ mm the lowest laser power is $P = 1180$ W, at which the hardening temperature of $T = 969$°C on the surface was obtained.
- Third optimization showed that for the sample with the thickness of $t = 3$ mm, the slowest scanning speed is $v = 4$ mm/s and at the same time the weakest laser power $P = 990$ W, which allows to obtain a temperature of $T = 963$°C on the sample surface, which is in the hardening range.

Each of the optimizations performed confirmed that the combination of a genetic algorithm with DT

in the form of a neural network is an extremely effective tool for planning the hardening process. Instead of time-consuming simulations or expensive laboratory tests, a few evolutionary iterations are enough to select the best hardening conditions. All key technological and physical constraints are built directly into the evaluation function, which ensures that the proposed parameters are immediately practically feasible. In addition, this approach allows for minimising energy and raw material consumption, while maintaining full process safety and the highest quality of the hardening process.

References

Baronti, L., Michalek, A., Castellani, M., Penchev, P., See, T. L., & Dimov, S. (2022). Artificial neural network tools for predicting the functional response of ultrafast laser textured/structured surfaces. *The International Journal of Advanced Manufacturing Technology*, *119*, 3501–3516. https://doi.org/10.1007/s00170-021-08589-9

Berkowski, L., & Borowski, J. (2007). Wpływ struktury na skutki azotowania chromowych stali ledeburytycznych. Część II. Warunki obróbki cieplnej stali NC10 [The influence of structure on the results of the nitriding of ledeburitic chromium steels. Part II. Heat treatment conditions of NC10 steel]. *Obróbka Plastyczna Metali*, *1*, 23–33.

Chen, G., Zhu, J., Zhao, Y., Hao, Y., Yang, Ch., & Shi, Q. (2021). Digital twin modeling for temperature field during friction stir welding. *Journal of Manufacturing Processes*, 64, 898–906. https://doi.org/10.1016/j.jmapro.2021.01.042

Czupryński, A., Janicki, D., Górka, J., Grabowski, A., Wyględacz, B., Matus, K., & Karski, W. (2022). High-power diode laser surface transformation hardening of ferrous alloys. *Materials*, *15*(5), 1915. https://doi.org/10.3390/ma15051915

Derlatka, A., & Lacki, P. (2024). Experimental study and numerical simulation of cellular I-beam manufactured using refill friction stir spot welding technology. *Thin-Walled Structures*, *200*, 111890. https://doi.org/10.1016/j.tws.2024.111890

Hegedűs-Kuti, J., Szőlősi, J., Birosz, M. T., Csobán, A., Popa-Müller, I., & Andó, M. (2025). Extending the welding seams detection as preparation towards the digital twin technology. *IET Collaborative Intelligent Manufacturing*, *7*(1), https://doi.org/10.1049/cim2.70027

Lacki, P., Derlatka, A., Więckowski, W., & Adamus, J. (2024). Development of FSW process parameters for lap joints made of thin 7075 aluminum alloy sheets. *Materials*, *17*(3), 672. https://doi.org/10.3390/ma17030672

Lesyk, D. A., Martinez, S., Mordyuk, B. N., Dzhemelinskyi, V. V., Lamikiz, A., & Prokopenko, G. I. (2019). Effects of laser heat treatment combined with ultrasonic impact treatment on the surface topography and hardness of carbon steel AISI 1045. *Optics & Laser Technology*, *111*, 424–438. https://doi.org/10.1016/j.optlastec.2018.09.030

Lesyk, D., Hruska, M., Mordyuk, B., Kochmanski, P., & Powalka, B. (2023). Robot-assisted 3D laser surface hardening of medium-carbon steel: Surface roughness parameters and hardness. In I. Karabegovic, A. Kovačević, S. Mandzuka (Eds.), *New Technologies, Development and Application VI* (vol. 1, pp. 45–53, Lecture Notes in Networks and Systems, vol. 687). Springer Cham. https://doi.org/10.1007/978-3-031-31066-9_5

Lv, T.-L., Xia, Y.-J., Murugan, S. P., Okigami, F., Ghassemi-Armaki, H., Carlson, B. E., & Li, Y. (2025). Multi-physical process simulation of resistance spot welding available for synthetic data generation. *Journal of Manufacturing Processes*, *141*, 709–724. https://doi.org/10.1016/j.jmapro.2025.03.024

Łach, Ł. (2024). Recent advances in laser surface hardening: Techniques, modeling approaches, and industrial applications. *Crystals*, *14*(8), 726. https://doi.org/10.3390/cryst14080726

Mahrle, A., & Beyer, E. (2019). Theoretical evaluation of radiation pressure magnitudes and effects in laser material processing. *Physica Scripta*, *94*, 075004. https://doi.org/10.1088/1402-4896/ab04c3

Mandolfino, C., Obeidi, M., Lertora, E., & Brabazon, D. (2020). Comparing the adhesion strength of 316L stainless steel joints after laser surface texturing by CO_2 and fiber lasers. *The International Journal of Advanced Manufacturing Technology*, *109*, 1059–1069. https://doi.org/10.1007/s00170-020-05639-6

Metzner, D., Olbrich, M., Lickschat, P., Horn, A., & Weißmantel, S. (2020). Experimental and theoretical determination of the effective penetration depth of ultrafast laser radiation in stainless steel. *Lasers in Manufacturing and Materials Processing*, *7*, 478–495. https://doi.org/10.1007/s40516-020-00129-9

Mu, H., He, F., Yuan, L., Commins, P., Wang, H., & Pan, Z. (2023). Toward a smart wire arc additive manufacturing system: A review on current developments and a framework of digital twin. *Journal of Manufacturing Systems*, *67*, 174–189. https://doi.org/10.1016/j.jmsy.2023.01.012

Mu, H., He, F., Yuan, L., Commins, P., Xu, J., & Pan, Z. (2025). High-frequency real-time bead geometry measurement in wire arc additive manufacturing based on welding signals. *IEEE Transactions on Industrial Informatics*, *21*(3), 2630–2639. https://doi.org/10.1109/TII.2024.3514121

Nayak, S. S., Iqbal, M. P., Krishna, A., Mishra, D., Pal, S. K., & Bhogineni, S. K. (in press). A hybrid digital twin for monitoring and controlling weld quality in friction stir welding. *International Journal of Computer Integrated Manufacturing*. https://doi.org/10.1080/0951192X.2025.2482227

Negri, E., Fumagalli, L., & Macchi, M. (2017). A review of the roles of Digital Twin in CPS-based production systems. *Procedia Manufacturing*, *11*, 939–948. https://doi.org/10.1016/j.promfg.2017.07.198

Pakieła, W., Tanski, T., Brytan, Z., Chladek, G., & Pakieła, K. (2020). The impact of laser surface treatment on the microstructure, wear resistance and hardness of the AlMg5 aluminum alloy. *Applied Physics A*, *126*, 231. https://doi.org/10.1007/s00339-020-3350-x

Pawłowicz, W. (2014). Hardening with high-power diode laser. *Welding International*, *28*(9), 679–682. https://doi.org/10.1080/09507116.2012.753225

Rauch, Ł., Bzowski, K., Szeliga, D., & Pietrzyk, M. (2020). Development and application of the statistically similar representative volume element for numerical modelling of multiphase materials. In V. V. Krzhizhanovskaya, G. Závodszky, M. H. Lees, J. J. Dongarra, P. M. A. Sloot, S. Brissos, J. Teixeira (Eds.), *Computational Science – ICCS 2020. 20th International Conference, Amsterdam, The Netherlands, June 3–5, 2020, Proceedings* (part VI, pp. 389–402, Lecture Notes in Computer Science, vol. 12142). Springer Cham. https://doi.org/10.1007/978-3-030-50433-5_30

Schüßler, P., Damon, J., Mühl, F., Dietrich, S., & Schulze, V. (2023). Laser surface hardening: A simulative study of tempering mechanisms on hardness and residual stress. *Computational Materials Science*, *221*, 112079. https://doi.org/10.1016/j.commatsci.2023.112079

Sharma, A., Kosasih, E., Zhang, J., Brintrup, A., & Calinescu, A. (2022). Digital Twins: State of the art theory and practice, challenges, and open research questions. *Journal of Industrial Information Integration*, *30*, 100383. https://doi.org/10.1016/j.jii.2022.100383

Szczucka-Lasota, B., Uściłowska, A., Węgrzyn, T., & Węgrzyn-Wolska, K. (2025). Aluminum busducts welding with micro-jet cooling-process parameters estimation by numerical simulations with MFS. *Continuum Mechanics and Thermodynamics*, *37*, 14. https://doi.org/10.1007/s00161-024-01351-y